COMMUNICATION

🅡 Check for updates

Efficient electrocatalytic reduction of CO_2 to CO enhanced by the synergistic effect of N,P on carbon aerogel†

Yifan Yan,[a] Hongzhi Wang,*[b] Xinze Bi,[a] Yuezhu Zhao[a] and Mingbo Wu 🆔 *[a]

A metal-free catalyst, N,P-codoped carbon aerogel, was used to realize the high efficiency reduction of CO_2 to CO. Therein, the pyridinic N acts as the active center to activate and reduce CO_2 and the atom of P acts as the "transition atom" of the proton to reduce the free energy barrier from *CO_2 to *COOH.

The increasing concentration of carbon dioxide (CO_2) in the atmosphere has caused a series of environmental problems, such as global warming, ocean acidification and so on.[1–3] One of the most economical and effective ways to change this phenomenon is to convert CO_2 into high value-added chemicals using renewable electricity.[4] However, there are various issues that currently impose restrictions on its practical application, including low reactivity, poor stability and high cost.[5–7] Aerogels are widely used as catalysts because of their porous structure,[8] which can expose more active sites and enhance the reactivity.[9,10] In recent years, researchers have used this characteristic to develop aerogels for the CO_2 reduction reaction (CO_2RR), including single metallic aerogels,[11] alloy aerogels,[12] bimetallic aerogels,[13] and composite aerogels.[14]

Recently, carbon-based materials have been widely used because of their good electrical conductivity, excellent stability, extensive resources and low cost.[15,16] Carbon aerogels exhibit all the advantages of carbon-based materials and aerogels, and are highly studied due to their customizable physical and chemical properties.[17] However, the performance of the CO_2RR is still unsatisfactory due to the poor reactivity resulting from the fewer active sites. In order to increase the number of active sites, various methods have been tried to modify the carbon aerogels. Doping is considered to be one of the effective methods to improve the activity of the CO_2RR. Compared with

doping metal catalysts, metal-free catalysts have the advantages of low cost and high stability. Therefore, researchers have focused on developing doping metal-free carbon aerogels as catalysts in recent years. Nevertheless, in the field of the CO_2RR, due to the low proton transfer rate on carbon aerogel, the intermediate barrier of $CO_2 \rightarrow$ *COOH is too high, which negatively affects the product yield. According to previous reports,[18,19] pyridine N is a favorable catalytic active site because of its low free energy barrier for the formation of a *COOH intermediate. On the other hand, P doping usually occurs at the edge of the carbon plane, which leads to structural distortion. Based on this, P doping can significantly increase the specific surface area of the catalyst. Meanwhile, as a "transition atom" of *H, P can reduce the *CO_2 + *H $\rightarrow$ *COOH energy barrier and accelerate CO_2RR to produce CO.

Here, four different catalysts, doped with different non-metallic elements (N and/or P), were prepared by using porous carbon aerogel as a carbon skeleton carrier. At the same time, the ratio of N and P was studied in detail to maximize the synergy between N and P in NPCA. During the CO_2RR, N element worked as the main active site. In particular, pyridine N can catalyze the conversion of CO_2 to CO. Besides, P element can promote the formation of porous structures, thus exposing more active sites.

Fig. 1a shows the schematic diagram of the synthesis of N,P-codoped carbon aerogel (NPCA). Meanwhile, carbon aerogel (CA), N-doped carbon aerogel (NCA) and P-doped carbon aerogel (PCA) were also prepared as control samples by simply changing the raw materials. The only difference between these samples is whether urea and phytic acid were added during the preparation process. The scanning electron microscope (SEM) images of the catalysts are shown in Fig. 1b–e. It can be seen that the four catalysts exhibit similar porous honeycomb-like structures, which consist of graphene-like flexible nanosheets. The model diagram at the upper right corner can also clearly reflect the morphological changes of each sample. Meanwhile, the thickness of the nanosheets that make up the samples is also different (Fig. S1, ESI†). The nanosheets of the PCA sample

[a] *College of New Energy, State Key Laboratory of Heavy Oil Processing, China University of Petroleum (East China), Qingdao 266580, China. E-mail: wumb@upc.edu.cn*

[b] *College of Chemistry and Chemical Engineering, Ocean University of China, Qingdao, 266100, China. E-mail: wanghz@ouc.edu.cn*
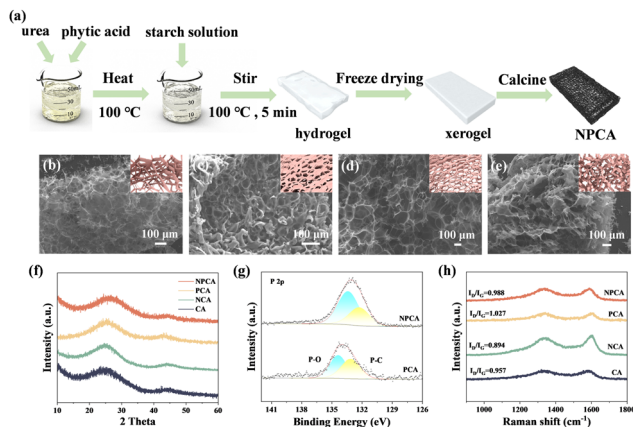
Fig. 1 (a) Detailed preparation process of NPCA. The SEM image of CA (b), NCA (c), PCA (d), and NPCA (e). The model diagrams are shown in the upper right corner. The XRD patterns (f), P 2p XPS spectra of PCA and NPCA (g), and Raman spectra (h).

Fig. 2 (a) FEs and product distributions at various potentials. Partial current densities for CO (b) and H_2 (c) of the four catalysts. Tafel plots (d), Nyquist plots (e), and capacitive currents with different sweep rates (f) of CA, NCA, PCA, and NPCA.

show the thinnest morphology, followed by CA, NPCA and NCA (Fig. S2, ESI†), which may result from the doping of P. The catalysts were further characterized by X-ray diffraction (XRD) to confirm the crystal structure. As shown in Fig. 1f, all catalysts exhibit two broad diffraction peaks around 24° and 44°, corresponding to the (002) and (100) planes of carbon. The samples were further investigated by X-ray photoelectron spectroscopy (XPS) to comprehend the surface composition and chemical properties. The XPS results show that P 2p spectra can be assigned to carbon-bonded phosphorus (P–C) and oxidized phosphorus (P–O) species (Fig. 1g and Fig. S3, ESI†). Since P (χ = 2.19) is less electronegative than C (χ = 2.55), the P–C bond can change the charge and spin density of carbon, resulting in structural defects of carbon materials.[20] The Raman spectra further prove the phenomenon (Fig. 1h). The two peaks located at around 1340 cm^{-1} and 1580 cm^{-1} corresponded to the D band and G band, respectively. It is worth noting that NPCA presents the I_D/I_G ratio of 0.988, ranking only second to PCA (1.027). The I_D/I_G ratios for CA and NCA were 0.957 and 0.894, respectively. The results fully prove that more defects were introduced by doping P, while N doping would reduce defects.[21]

After resolving the structural information of the catalysts, the electrochemical properties of the four samples were measured in a typical H-cell with a standard three-electrode system. It is worth noting that these four catalysts can be used directly as electrodes without the cumbersome process of preparing ink solution and dropping electrodes, which is crucial to enhance the stability. Linear sweep voltammetry (LSV) is first applied to evaluate the CO_2RR performance. As shown in Fig. S4 (ESI†), NPCA exhibits the lowest initial potential, indicating that NPCA was the most likely to activate CO_2. The selectivity of the products under various potentials was investigated and the obtained gas and liquid products were directly quantified by online gas chromatography and liquid chromatography, respectively. Fig. 2a shows that the gas products are only H_2 and CO, and no liquid products were detected. It can be seen that the FE
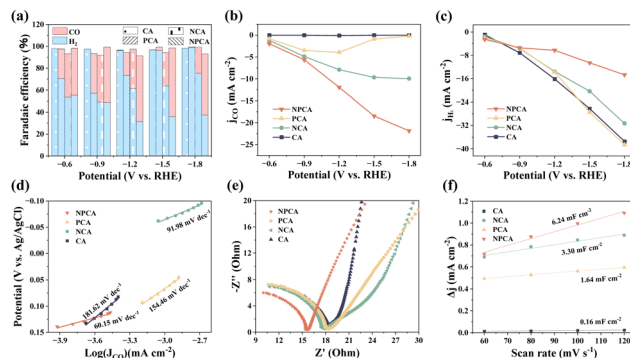
of CO (FE_{CO}) for NPCA is the highest among the four samples at all detected potentials (− 0.6 to −1.8 V vs. RHE). This indicates that N,P-codoped could significantly improve the performance of the CO_2RR. Meanwhile, the performance of NPCA is better than that of NCA indicating that the active sites doped with N,P are more numerous than those doped only with N. To further verify this conclusion, N_2 adsorption–desorption measurements were performed on NCA and NPCA (Fig. S5, ESI†). The results show that NPCA has a larger specific surface area than NCA, which is conducive to exposing more active sites. The corresponding pore size distribution curves indicate that NPCA is enriched with a large number of microporous structures, which is consistent with Fig. S5a (ESI†). At the same time, the partial current density of CO (j_{CO}) was calculated (Fig. 2b). The j_{CO} of NPCA is significantly higher than that of NCA, PCA and CA at the same potential, and its maximum value can reach up to −21.82 mA cm^{-2} at −1.8 V (vs. RHE). In addition, both CA and PCA showed strong H_2 production capacity, while j_{H_2} of NPCA is the lowest (Fig. 2c).

The intrinsic reason for enhancing the CO_2RR by N,P-codoping was further explored. As shown in Fig. 2d, NPCA exhibits the lowest Tafel slope among the four catalysts, which indicates that the synergistic effect of N and P could accelerate the reaction kinetics. The internal charge transfer resistance (R_{ct}) of the prepared samples at open circuit potential was further employed by electrochemical impedance spectroscopy (EIS). The Nyquist plots are shown in Fig. 2e, where it can be clearly observed that NPCA exhibits the lowest interfacial R_{ct}, suggesting that the NPCA catalyst could promote charge transfer and improve the performance of the CO_2RR. Meanwhile, the double layer capacitance (C_{dl}) was calculated by cyclic voltammograms (CV) at varying scanning rates (Fig. S6, ESI†). Fig. 2f shows that the NPCA exhibits a larger C_{dl} than PCA, NCA, and CA, which indicates that the electrochemical active surface area (ECSA) of NPCA is the biggest among the four catalysts,[22] which is consistent with the results shown in Fig. 2a.
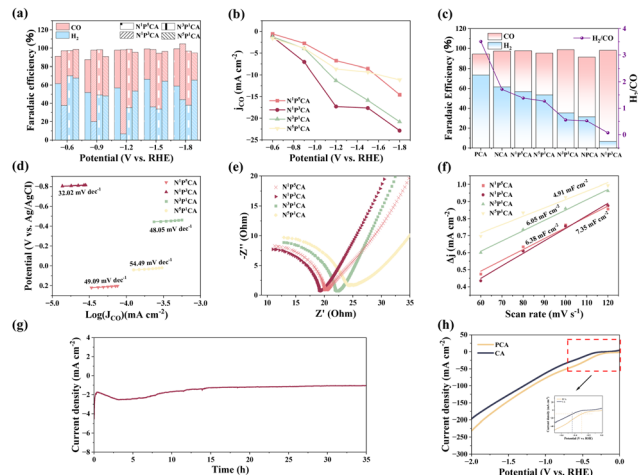
Benefiting from the synergistic effect of N and P, the performance of CO_2RR for NPCA improved within a certain range. However, the FE_{CO} of NPCA is still unsatisfactory.
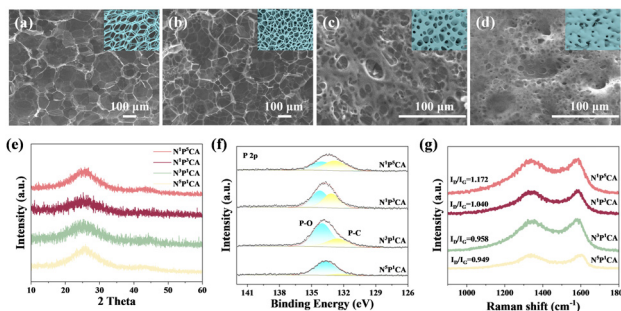
Fig. 3 The SEM images of N^1P^5CA (a), N^1P^3CA (b), N^3P^1CA (c), and N^5P^1CA (d). The N^1P^5CA, N^1P^3CA, N^3P^1CA, and N^5P^1CA model diagrams are shown in the upper right corner of the images. The XRD patterns (e), P 2p XPS spectra of samples with different N,P doping amounts (f), and Raman spectra (g).

Fig. 4 (a) FEs for four samples under various potentials. (b) Partial current densities for the CO products over the different catalysts. (c) FE_{CO}, FE_{H_2}, and H_2/CO ratios of PCA, NCA, N^1P^5CA, N^5P^1CA, N^3P^1CA, NPCA, and N^1P^3CA at -1.2 V (vs. RHE). Tafel plots (d), Nyquist plots (e), and capacitive currents with different sweep rates (f) of samples with different N,P doping amounts. (g) Chronopotentiometry test for N^1P^3CA at -1.2 V (vs. RHE) for 35 hours. (h) LSV curves of CA and PCA in 1 M Na_2SO_4 electrolyte.

According to the above SEM images, it can be obviously found that the morphology of NCA is significantly different from that of CA, and the pore wall is thicker. Therefore, we speculated that with the increasing amount of N doping, the pore wall will become thicker and the porous structure will gradually disappear, which is not conducive to the mass transfer process and the exposure of the active sites. Therefore, N as the active site is not doped as much as possible. The introduction of P can optimize the aerogel structure to expose more active sites and enhance the performance of the CO_2RR. Therefore, we consider whether the doping amounts of N and P can be adjusted to achieve the strongest synergistic effect of N and P.

Four catalysts, N^1P^5CA, N^1P^3CA, N^3P^1CA, and N^5P^1CA, were prepared by changing the addition amount of urea and phytic acid, and their morphology and structure were observed by SEM. As shown in Fig. 3a–d, the porous structure of the aerogels gradually disappeared with the increase in the amount of doping N element, which confirmed our conjecture above. The model diagram in the upper right corner of the SEM images can also clearly reflects the morphological and structural changes of the aerogel with the change in doping amount of N and P. The structure of CA gradually resembles a honeycomb with the augmentation of the P doping amount in a certain range. It could increase the surface area of CA effectively, which is conducive to exposing more active sites. Fig. S7 (ESI†) also clearly shows the obvious changes in the morphology of the four catalysts with different ratios of N and P. The XRD pattern also shows two wide diffraction peaks at around $24°$ and $44°$, corresponding to two planes of carbon, respectively (Fig. 3e), which is consistent with the result shown in Fig. 1f. Fig. S8 (ESI†) shows that there are C, N and P elements in N^1P^5CA, N^1P^3CA, N^3P^1CA, and N^5P^1CA. Meanwhile, the N 1s spectra display the presence of pyridinic N and graphitic N in all four samples. It can be seen that the P–C bond decreases with the decrease of P incorporation (Fig. 3f), which means fewer carbon defects. As shown in Fig. 3g, the N^1P^5CA exhibits the largest I_D/I_G ratio (1.172), which means that N^1P^5CA shows the most defects and N^1P^3CA (1.040) takes second place, which is conducive to the transport of electrons.

Similarly, the catalytic properties of samples doped with different amounts of N and P were determined using the electrochemical measurement method described above. As shown in Fig. S9 (ESI†), the initial potentials for N^5P^1CA and N^3P^1CA are both lower than that of N^1P^3CA and N^1P^5CA, which fully indicated that more amount of N doping was useful for the CO_2RR and N atoms may act as the active sites during the reduction reaction. During the CO_2RR, only CO and H_2 were detected by gas chromatography, and no liquid products were detected from liquid chromatography. As shown in Fig. 4a, the sample N^1P^3CA exhibits higher selectivity for CO than the other three catalysts. In addition, FE_{CO} performs up to 91.44% at -1.2 V (vs. RHE). This indicates that the amount of N and P doped in the catalyst is just enough to exert the maximum synergistic effect of N and P. Surprisingly, the N^5P^1CA sample doped with more N atoms than N^3P^1CA contains more active sites, but they are worse than N^3P^1CA at -0.9 V to -1.8 V (vs. RHE), which fully demonstrates the importance of having a high specific surface area to expose the active sites during the CO_2RR process. For the N^1P^5CA catalyst, there are not enough active sites to generate *COOH intermediates, so it reveals poor performance. The j_{CO} of these four catalysts was also calculated (Fig. 4b). Notably, the j_{CO} value of N^1P^3CA is as high as -22.86 mA cm^{-2} at -1.8 V (vs. RHE), which is 1.57 times, 1.1 times and 2.06 times that of N^1P^5CA, N^3P^1CA and N^5P^1CA at the same potential, respectively. Fig. 4c shows the H_2/CO ratio of seven different catalysts at -1.2 V (vs. RHE). It can be seen that the ratio of H_2/CO varies from 0.072 to 3.512 through changing the doping amount of N and P. In addition, we further discussed the internal factors of catalytic performance differences. As shown in Fig. 4d, the Tafel slopes of N^3P^1CA, N^5P^1CA, N^1P^3CA, and N^1P^5CA are 48.05, 54.49, 32.02, and 49.09 mV dec^{-1}, respectively. It indicates that N^1P^3CA displays
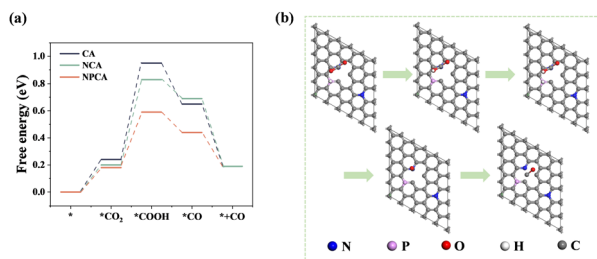
Fig. 5 (a) Free energy diagram for CO on CA, NCA and NPCA. (b) Schematic diagram of the model of the CO formation process on the NPCA catalyst.

good kinetic properties for the CO_2ER. The EIS shows that N^1P^3CA exhibits the minimum interfacial transfer resistance (Fig. 4e), indicating that it can efficiently reduce the interface energy barrier, and facilitate charge transfer. However, N^5P^1CA is the most difficult in charge transfer, which indirectly proves that the porous three-dimensional (3D) structures contribute to promoting charge transfer. N^1P^3CA presents the largest ECSA (Fig. 4f and Fig. S10, ESI†), manifesting that it can expose the most active sites to accelerate the CO_2ER. In summary, the reason for N^1P^3CA owning the best performance is that pyridine N is considered to be a favorable active site for the CO_2RR to CO, and doping of P could make the carbon aerogel form a porous honeycomb-like structure with high specific surface area and more exposed active sites. In addition, the optimal sample N^1P^3CA was tested electrochemically for up to 35 h (Fig. 4g). The result shows that it can maintain good current stability during testing. The characterization of N^1P^3CA after 35 h of electrolysis at -1.2 V indicates that the morphology (Fig. S11a, ESI†), the phase (Fig. S11b, ESI†) and the degree of carbon defects (Fig. S11c, ESI†) remain largely unchanged, which demonstrates that N^1P^3CA can maintain good stability during the CO_2ER. In order to further clarify the effect of the introduction of P on the CO_2RR, CA and PCA were used as working electrodes, and 1 M Na_2SO_4 was used as the electrolyte to determine the performance of the catalysts. As shown in Fig. 4h, the hydrogen evolution reaction (HER) overpotential of PCA is significantly lower than that of CA, which fully indicates that the introduction of P could accelerate proton transport.

In order to further understand the mechanism source of good selectivity for CO of NPCA and the synergistic effect between N and P elements, density functional theory (DFT) calculation was performed. As shown in Fig. 5a, NCA was more likely than CA to activate CO_2 for the next reaction to produce the key intermediate *COOH, but the free energy barrier of the adsorbed *COOH and *H combined to form *CO intermediates is higher, which was not conducive to CO production. Therefore, P atoms were introduced to promote the CO_2RR. The results show that after the introduction of a P atom, the free energies of *COOH generation decreased significantly, because P atoms, as the "transition atoms" of *H, could accelerate proton transfer. Fig. 5b shows the model diagram of the CO generation process in NPCA. CO_2 is first activated by the

N atom, and then combined with protons transported by the P atom to produce *COOH; *COOH then combined with protons to produce *CO after dehydration, and finally *CO desorption produced CO.

In summary, we prepared a N,P co-doped carbon aerogel for CO_2 reduction to CO. As the main active center, pyridinic N activates CO_2 and combines with a proton to produce *COOH, and finally produces the CO product. The introduction of P causes the aerogel to form a honeycomb porous structure, which increases the degree of carbon defects and accelerates proton transport. In order to maximize the synergistic effect of N and P, we prepared different proportions of catalysts by adjusting the doping amount of N and P. Among them, N^1P^3CA showed good catalytic performance due to its fastest proton transfer rate and the most active sites. The FE_{CO} is high, up to 91.44% at -1.2 V (vs. RHE), and it can maintain good current stability within 35 h. DFT calculations show that CO_2 molecules adsorbed on pyridinic N combine with a proton transported by P to form a *COOH intermediate, which greatly reduces the free energy barrier of the process. This study provides a promising method for the CO_2RR to give full play to the role of N and P atoms, and cooperate N and P to maximize the reduction of CO_2 to CO.

Conflicts of interest

There are no conflicts to declare.

Notes and references

1 X. Bi, et al., Energy Mater. Adv., 2023, 4, 0037.
2 X. Bi, et al., Energy Fuels, 2022, 36, 7206–7212.
3 Y. Yan, et al., Electron, 2023, 1, e3.
4 H. Wang, et al., Adv. Funct. Mater., 2023, 33, 2214946.
5 X. Kong, et al., J. Am. Chem. Soc., 2023, 145, 14903–14911.
6 L.-P. Chi, et al., Nat. Commun., 2021, 12, 12.
7 D.-S. Huang, et al., ACS Catal., 2022, 12, 8444–8450.
8 J.-H. Lee and S.-J. Park, Carbon, 2020, 163, 1–18.
9 Z. Zhang, et al., Chem. Eng. J., 2024, 479, 147376.
10 Y. L. Yang, et al., Adv. Mater., 2022, 34, e2206706.
11 P. Li, et al., Chem. Sci., 2023, 14, 310–316.
12 H. Li, et al., Adv. Mater., 2022, 35, 2209242.
13 Z. Wu, et al., Angew. Chem., Int. Ed., 2021, 60, 12554–12559.
14 Z. Zhong, et al., Appl. Catal., B, 2023, 330, 122603.
15 S. Gong, et al., Small, 2023, 19, 2207808.
16 Z. Gao, et al., Chin. Chem. Lett., 2022, 33, 2270–2280.
17 A. M. ElKhatat and S. A. Al-Muhtaseb, Adv. Mater., 2011, 23, 2887–2903.
18 C. Chen, et al., Angew. Chem., Int. Ed., 2020, 59, 11123–11129.
19 X. Liang, et al., ACS Sustainable Chem. Eng., 2022, 10, 1880–1887.
20 J.-Y. Hong, et al., Phys. Chem. Chem. Phys., 2015, 17, 30946–30962.
21 X. Xiao, et al., J. Colloid Interface Sci., 2019, 545, 1–7.
22 H. Liu, et al., ACS Appl. Mater. Interfaces, 2019, 11, 15528–15536.